

NUMERICAL INVESTIGATION OF TURBULENT OPEN CHANNEL FLOW OVER A PERMEABLE BED: PORE-RESOLVED SIMULATIONS AND UPSCALED MODELING

Shashank Karra

School of Mechanical, Industrial, and Manufacturing Engineering
Oregon State University
204 Rogers Hall,
Corvallis, OR 97331
email: karras@oregonstate.edu

Sourabh V. Apte

School of Mechanical, Industrial, and Manufacturing Engineering
Oregon State University
204 Rogers Hall,
Corvallis, OR 97331
email: sva@oregonstate.edu

ABSTRACT

Numerical investigations of the interactions between streamflow turbulence and groundwater flow through a randomly packed porous sediment bed is performed at a permeability Reynolds number, Re_K , of 2.56. Pore-resolved, direct numerical simulation (DNS) data from a recent study (Karra *et al.*, 2023) is used to assess the predictive capability of an upscaled, continuum model based on the method of volume averaging. A spatially varying porosity profile generated from the pore-resolved DNS is matched with a fifth-order polynomial to obtain smoothly varying porosity in the bed-normal direction for the continuum approach. Volume-averaged Navier-Stokes (VaNS) equations are solved with a model for the drag force in the porous bed based on the modified Ergun equation with Forchheimer corrections for inertial terms. The upscaled, VaNS model is shown to capture the flow statistics and the bed-shear stress at the sediment-water interface accurately. Comparison of pressure fluctuations at the sediment-water interface shows a slight underprediction with the VaNS model compared to the pore-resolved study. This is attributed to the local protrusions of the sediment particles present in the pore-resolved study, but absent in the continuum model.

INTRODUCTION

Interchange of mass and momentum between surface water and ground water occurs in the porous bed beneath the streams, termed as the hyporheic zone. This exchange of mass and momentum (hyporheic exchange) of solutes such as chemicals and pollutants, dissolved oxygen, nutrients, and heat across this zone is a critical component in sustaining diverse aquatic ecosystems. The penetration of mean and turbulent flow within the porous bed and near bed pressure fluctuations have been identified (Hester *et al.*, 2017) to play a

crucial in understanding this hyporheic exchange. While there are many parameters which characterize exchange of mass and momentum across the sediment water interface (SWI), the permeability Reynolds number, representing the ratio between the permeability scale to the viscous scale $\sqrt{K}/(\nu/u_\tau)$, where K is the permeability, ν is the kinematic viscosity, and u_τ is the friction velocity, is typically used to identify different flow regimes. Based on the characterization by Voermans *et al.* (2017); Grant *et al.* (2018) turbulence is dominant near the SWI for $Re_K > 1$.

Karra *et al.* (2023) developed pore-resolved DNS data for turbulent flow over a randomly packed, monodispersed, sediment bed at three different Re_K values of 2.56, 5.17, and 8.94, representative of natural stream or river systems. Time-space averaging was used to quantify the Reynolds stress, form-induced stress, mean flow and shear penetration depths, and mixing length at the sediment-water interface (SWI). The mean flow and shear penetration depths increase with Re_K and were found to be nonlinear functions of non-dimensional permeability. The peaks and significant values of the Reynolds stresses, form-induced stresses, and pressure variations were shown to occur in the top layer of the bed. They also quantified the differences in turbulence structure and pressure fluctuations between the randomly packed porous sediment beds and rough, impermeable walls with roughness characteristics derived from the top layer of the sediment bed. It was shown that turbulence structures in the free stream and pressure fluctuations at the sediment-water interface (SWI) are better captured by considering at least the top layer of sediment bed.

Although pore-resolved numerical experiments provide very detailed flow field and pressure data, the computational power and time needed are enormous. The present study aims at developing an upscaled continuum model based on the method of volume-averaging developed by (Whitaker, 1996). The resulting volume-averaged Navier-Stokes (VaNS) equations are solved and the results are validated against the pore-

resolved DNS data. The continuum VaNS approach is efficient and computationally cheaper and thus can be applied to reach scale modeling of hyporheic exchange at much larger $Re_K \sim \mathcal{O}(50 - 100)$ for flatbeds as well as turbulent flows over permeable, bedforms. .

MATHEMATICAL FORMULATION

Similar to the large-eddy simulation (LES) formulation, in volume-averaged Navier-Stokes (VaNS) equations, a representative elementary volume (REV) with length scale larger than the pore/particle size and smaller than bed thickness is used for volume averaging. The filter in VaNS equations; however, remains constant even near a sediment boundary, unlike typical LES formulation where the filter scale is decreased near a physical boundary. The VaNS equations are valid over the entire free stream, permeable bed and stream-bed interface regions and are given as (Breugem *et al.*, 2006; Rosti *et al.*, 2015)

$$\nabla \cdot \langle \theta \mathbf{u} \rangle = 0, \quad (1)$$

$$\frac{\partial \langle \mathbf{u} \rangle}{\partial t} + \frac{1}{\theta} \nabla \cdot [\theta \langle \mathbf{u} \rangle \langle \mathbf{u} \rangle] + \frac{1}{\theta} \nabla \cdot [\theta \boldsymbol{\tau}] = -\frac{1}{\theta \rho} \nabla [\theta \langle p \rangle] + \frac{\nu}{\theta} \nabla^2 [\theta \langle \mathbf{u} \rangle] + \mathbf{f} \quad (2)$$

$$\boldsymbol{\tau} = \langle \mathbf{u} \mathbf{u} \rangle - \langle \mathbf{u} \rangle \langle \mathbf{u} \rangle \approx \langle \widetilde{\mathbf{u} \mathbf{u}} \rangle \quad (3)$$

$$\mathbf{f} = \underbrace{-\nu \mathbf{K}^{-1} \theta \langle \mathbf{u} \rangle}_{\text{Darcy}} - \underbrace{\nu \mathbf{K}^{-1} \theta \langle \mathbf{u} \rangle \mathbf{F}}_{\text{Forchheimer Correction}} \quad (4)$$

where $\langle \rangle$ represents volume averaging, $\widetilde{(\)}$ represents subfilter scale fluctuations, θ is the porosity, $\boldsymbol{\tau}$ is the subfilter scale stress, which is similar to the subgrid-scale stress in LES, and \mathbf{f} is the drag force per unit mass the solid phase exerts on the fluid phase. The drag force consists of a Darcy term with permeability tensor (\mathbf{K}) and a Forchheimer correction tensor for inertial and turbulent fluctuations (\mathbf{F}). The Darcy and Forchheimer correction terms are modeled using the widely used Ergun relation with correlation coefficients determined from a wide range of experimental data (Breugem *et al.*, 2006),

$$\mathbf{K} = \frac{D_p^2 \theta^3}{\mathcal{A}(1-\theta)^2} \mathbf{I}, \quad \mathbf{F} = \tilde{F} |\langle \mathbf{u} \rangle| \mathbf{I}, \quad \tilde{F} = \frac{\theta}{\mathcal{B}(1-\theta)} \frac{D_p}{\nu}, \quad (5)$$

where D_p is the effective diameter of the solid beads. In the present study $\mathcal{A} = 180$ and $\mathcal{B} = 100$ is used (Macdonald *et al.*, 1979; Breugem *et al.*, 2006).

The subfilter scale stress can be modeled using typical subgrid scale models used in large-eddy simulation (such as the dynamic Smagorinsky model); however, this term is found to be small within the porous bed. In addition, since the grid resolution in the free-stream is equivalent to DNS resolution typically used for channel flows, the subfilter scale stress is neglected throughout the domain.

Numerical Approach

The numerical approach is based on Cartesian, rectilinear grids with smooth variation in grid resolution across the SWI. A fully parallel, structured, collocated grid, fractional time-stepping based finite volume solver has been developed and used for these simulations. The drag force term in the porous

regime is treated implicitly using Crank-Nicholson, which provides significant robustness and avoids very small computational time steps especially for cases with small effective permeability.

Computational Parameters

Direct simulations of turbulent flow over a permeable bed (PB-DNS), an impermeable rough wall with surface roughness elements identical to the top layer of the permeable bed (IWF-DNS), a smooth, impermeable wall (SW-DNS), and flow over permeable bed simulated using the present VaNS model (PB-VaNS) were performed. The flow configurations are shown in figure 1. The computational domain used in the pore-resolved PB-DNS simulation is composed of four layers of mono-dispersed, randomly distributed particles as shown in figure 1a (see Karra *et al.* (2023, 2022); Karra (2023) for details). The computational domain is assumed periodic in the axial (main flow) and spanwise directions, slip condition is enforced at both the top and bottom boundaries. For IWF-DNS, only the top layer of the permeable bed is used with a no-slip wall underneath the top layer (figure 1b). A fictitious domain method devised to handle arbitrary shaped immersed objects without requiring the need for body-fitted grids (Apte *et al.*, 2009) is used for PB-DNS and IWF-DNS. For the smooth, impermeable wall (SW-DNS), standard open channel flow simulation is performed for the free-stream. Finally, for the PB-VaNS, the permeable bed is replaced by smoothly varying bed-normal porosity (figure 1c,d) and the flow within the bed experiences an additional drag force modeled by the Darcy-Forchheimer relation described earlier.

Table 1 shows the details of the simulation parameters for $Re_K = 2.56$, computational domain, and grid resolutions used for the PB-DNS, IWF-DNS, SW-DNS, and PB-VaNS computations at same friction Reynolds number (Re_τ). To capture the inertial flow features within the pore and around spherical particles, roughly 90 grid points per diameter of the particle are used in the bed-normal direction in the top layer of the particles. Bed-normal grid resolution is coarsened and stretched away from the top layer in the free-stream as well as within the bed. In the x and z directions, a uniform grid with about 26 points per-sediment grain are used to resolve the bed geometry, resulting in a very large computational grid of $1152 \times 350 \times 576$. For the IWF-DNS case, since only the top layer of sediment particles are used, $1152 \times 240 \times 576$ grid points are used.

Using the grid resolution as the filter for volume averaging, randomly distributed particle locations for the permeable bed and particle sizes are used to compute the local porosity which is averaged in the homogeneous directions to obtain the bed-normal porosity variation shown in figure 1c. A fifth-order polynomial fit is used to obtain a smooth variation of the bed-normal porosity in the sediment-water interface region for the VaNS computations as shown in figure 1b,

$$\theta(y) = 1 - 6(\theta_{\text{avg}} - 1) \left(\frac{y}{\delta_i} \right)^5 - 15(\theta_{\text{avg}} - 1) \left(\frac{y}{\delta_i} \right)^4 - 10(\theta_{\text{avg}} - 1) \left(\frac{y}{\delta_i} \right)^3, \quad (6)$$

where θ_c is the porosity within the bed. The above model for porosity requires the specification of the thickness, δ_i , of the interface region, which is obtained by matching the profile to the volume-averaged porosity in PB-DNS. The computational

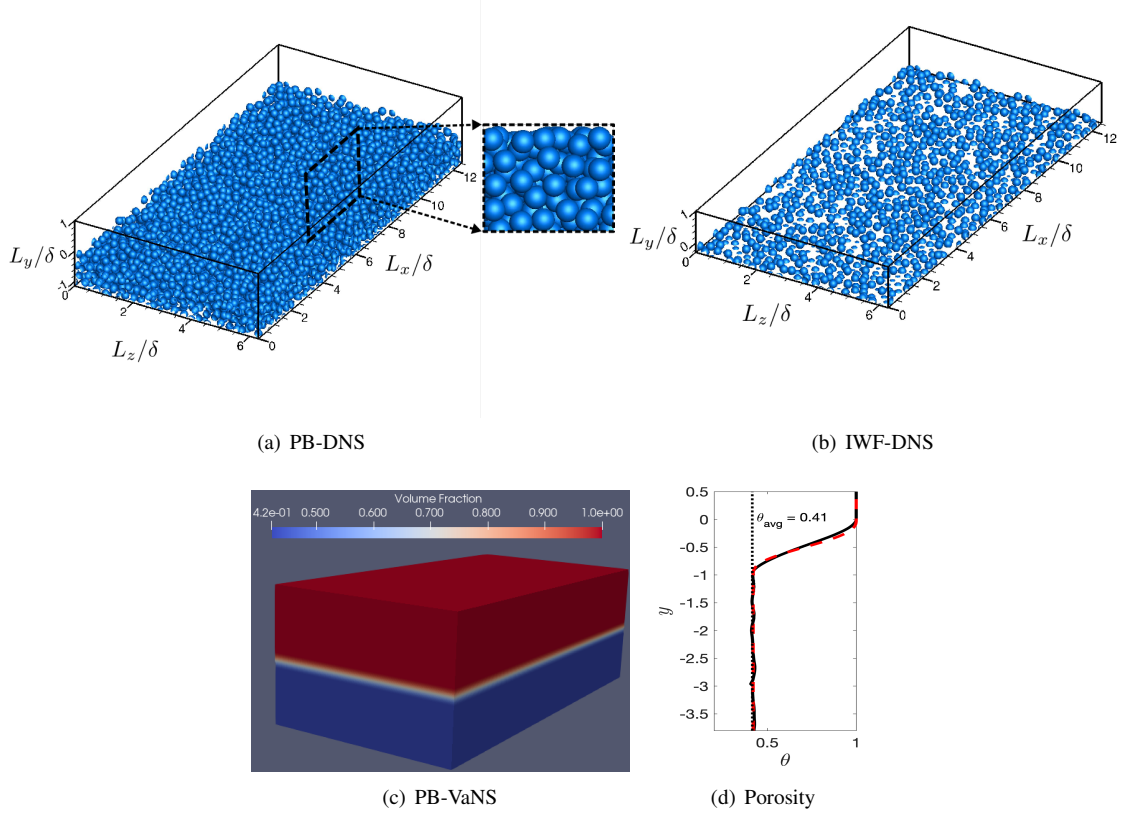


Figure 1. (a) Permeable bed with four layers of sediment particles (inset shows close-up view in xy -plane) for PR-DNS study, (b) impermeable rough wall with roughness characteristics identical to the top layer of the permeable bed, (c) porosity field used in VaNS simulation of permeable bed, and (d) comparison of bed-normal porosity variation (—) in the sediment bed obtained by volume averaging the pore-resolved data and fifth order polynomial fit (- -) used in the VaNS model.

Table 1. Parameters used in present direct numerical simulations where, D_p is the sphere diameter, δ is the free-stream height, H_s is the sediment depth, and θ_{avg} is the porosity within the bed. L_x and L_z are the streamwise and spanwise domain lengths, Re_K , Re_τ , Re_b and D^+ are the permeability, friction, bulk and roughness Reynolds numbers, respectively. $()^+$ denotes wall units.

Case	Re_K	Re_τ	Re_b	D^+	θ_{avg}	H_s/δ	D_p/δ	$(L_x, L_z)/\delta$	$(\Delta x^+, \Delta y^+, \Delta z^+)$
PB-DNS	2.56	270	2,826	77	0.41	1.14	0.29	$(4\pi, 2\pi)$	(2.94, 0.95, 2.94)
IWF-DNS	-	270	2,818	77	-	0.29	0.29	$(4\pi, 2\pi)$	(2.94, 0.95, 2.94)
SW-DNS	-	270	4,461	0	-	-	-	$(4\pi, 2\pi)$	(2.94, 0.95, 2.94)
PB-VANS	2.5	263	2,829	75	0.41	1.14	0.29	$(4\pi, 2\pi)$	(7.5, 0.95, 6.0)

grid for the VaNS calculation is coarser ($468 \times 250 \times 280$) and is also stretched in the bed-normal direction to maintain $y^+ < 1$ near the bed.

RESULTS AND DISCUSSION

The flow in the simulations is driven by a body force imposed to obtain a constant target mass flow rate. The target mass flow rate is adjusted till the desired friction velocity and $Re_K = \sqrt{K}u_\tau/\nu$ are obtained. The friction velocity, u_τ , is calculated from the maximum value of the time-space averaged total stress. The friction Reynolds number is based on the free-stream height (δ) and is given as $Re_\tau = u_\tau\delta/\nu$. It should be noted that for PB-DNS and IWF-DNS, the friction velocity, u_τ , is calculated from the maximum value of the time-space averaged total stress equation, which is defined as sum

of the viscous stress, turbulent shear stress, and the dispersive or form-induced shear stress (Nikora *et al.*, 2004),

$$\tau(y) = \underbrace{\rho\nu\partial(\theta\langle\bar{u}\rangle)/\partial y}_{\text{viscous}} - \underbrace{\rho\theta\langle u'v' \rangle}_{\text{turbulent}} - \underbrace{\rho\theta\langle \bar{u}\bar{v} \rangle}_{\text{dispersive}}. \quad (7)$$

In the VaNS computations, since the porosity is assumed uniform in the spanwise and axial flow directions, the dispersive stresses are absent. The computations are first carried out for 20-25 flow-through times (computed as the length over average bulk velocity L_x/U_b) to obtain a stationary turbulent flow. Single-point and two-point statistics were then collected by computing for an additional time period of $T = 13\delta/u_\tau$.

Iso-surfaces of local swirling strength, λ_{ci} , defined as the imaginary part of the complex conjugate eigenvalue of the ve-

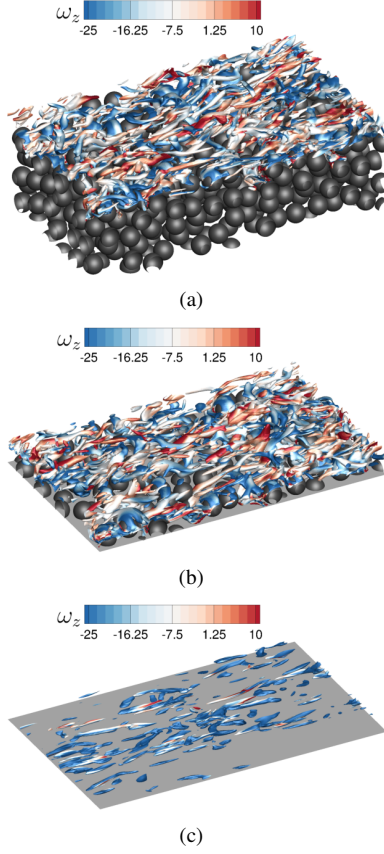


Figure 2. Iso-surface of swirling strength at $\lambda_{ci} = 0.1\lambda_{ci,max}$, colored by z -component of vorticity, ω_z , shown between $8.57 < x/\delta < 12.56$, $2.28 < z/\delta < 4.57$ and very close to the bed, $y/\delta < 0.057$ for (a) PB-DNS, (b) IWF-DNS, and (c) SW-DNS cases.

locity gradient tensor, $\partial_{x_j}u_i$, are shown in figure 2 to gain a qualitative insight into the differences in turbulence structures between the permeable bed, impermeable rough wall, and smooth wall cases. The isosurfaces in figure 2 are set at 10% of the maximum value of λ_{ci} and contours are colored by the z -component of vorticity, ω_z . The PB-DNS and IWF-DNS cases show very similar vortical structures with a wide range of sizes. This suggests that the top layer of the bed strongly impacts the coherent structures. The smooth, impermeable wall shows long elongated structures indicative of strong anisotropy, whereas the porous bed and roughness elements break down these elongated flow structures and reduce the level of anisotropy.

Figure 3 shows the comparison of time-space averaged normalized mean velocity, bed-normal component of Reynolds stress, and bed-normal component of dispersive stress for the PB-DNS, IWF-DNS, and SW-DNS cases. The variables are normalized by the friction velocity, u_τ , and y is normalized by δ . Compared to the smooth wall case, the permeable and the impermeable rough wall cases show a mean velocity deficit due to fluid momentum loss. The permeable bed and impermeable full-layer cases show almost the same magnitudes of mean velocity and Reynolds stresses at the sediment crest. This shows that the presence of a solid wall underneath the full layer of spherical roughness elements has minimal influence on both mean flow field and turbulent fluctuations. The penetration of mean and turbulent fluctuations is thus restricted to the top layer of the bed for the permeability Reynolds num-

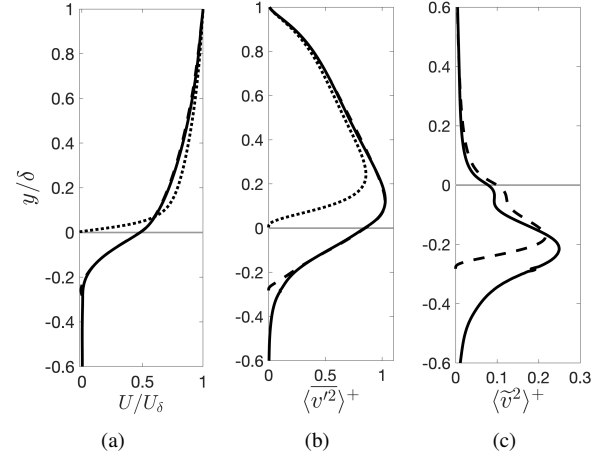


Figure 3. Comparison of the axial mean velocity, bed-normal turbulent stress, and bed-normal form-induced stress profiles for PB-DNS (—), IWF-DNS (---), and SW cases (···): (a) normalized axial mean velocity, (b) normalized bed-normal component of Reynolds stress, and (c) normalized bed-normal component of form-induced stress. Horizontal gray line (—) shows the crest of sediment bed for PB-DNS and IWF-DNS.

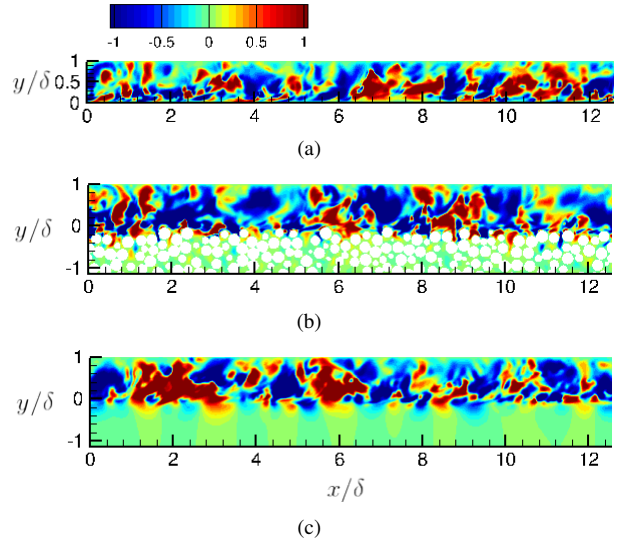


Figure 4. Contours of bed-normal velocity in the z -normal (symmetry) plane for (a) SW (b) PR-DNS and (b) VANS model.

ber investigated. The full layer of roughness elements creates pockets underneath where the flow can penetrate and since the turbulent kinetic energy within this layer is still small, the flow characteristics and momentum transport mechanisms resemble that of a permeable bed. Figure 3c shows the time-space averaged, bed-normal form-induced stresses ($\langle \tilde{v}^2 \rangle^+$) for the PB-DNS and IWF-DNS. Compared to the Reynolds stresses, the corresponding form-induced stresses are lower in magnitude, but show some differences in the peak value and its location, which occurs below the sediment crest. The form induced stresses are influenced by the solid underlying wall and flow penetration differs between the PB-DNS and IWF-DNS cases. This suggests that the impermeable, full layer of sediment roughness captures majority of the main effects of the permeable sediment bed, however, some form-induced effects

are not captured.

Figure 4 shows contours of instantaneous bed-normal velocity for the smooth wall (SW-DNS), the permeable bed (PB-DNS), and VaNS model (PB-VaNS), respectively, in the symmetry plane. Weakening of wall blocking effect due to bed permeability results in turbulent flow penetrating into the sediment bed in both PB-DNS and PB-VaNS cases. Regions of positive and negative bed-normal velocity values, in permeable bed cases, are associated with sweeps and ejections of fluid parcels which carry both momentum and mass in and out of the bed. The sweep and ejection events for permeable bed are found to be quite different than the impermeable, smooth wall case. The contours predicted by PB-VaNS are more diffused near the bed whereas in the pore-resolved case flow structures are broken down and distributed (or influenced) by the roughness element protrusions. The random distribution of roughness protrusions creates obstructions around and over which the turbulent flow mixing is more pronounced which leads to a greater spatial scale distribution in the pore-resolved case.

Figure 5 shows the time-space averaged mean velocity and Reynolds stresses for the three cases (SW-DNS, PB-DNS, and PB-VaNS). The variables are normalized by the friction velocity, u_τ , and y is normalized by free-stream height, δ . The profiles of mean velocity and Reynolds stresses for the PR-DNS and VaNS model compare well with each other. However, some differences are observed near the sediment crest, which are attributed to the effect of roughness protrusions on flow, which are absent in the VANS model. The roughness elements cause a slightly greater mean velocity deficit in the PR-DNS case. Compared to the smooth wall case though, both the permeable bed cases show a mean velocity deficit due to bed permeability and roughness caused momentum loss. For the VaNS model, the streamwise Reynolds stress, $\langle u'^2 \rangle^+$, shows slightly greater tangential spread near the crest, whereas the bed-normal Reynolds stress, $\langle v'^2 \rangle^+$ penetration below the crest is lower compared to PR-DNS. The random spread of the roughness protrusions in the top layer creates distinct channels through which flow can penetrate under the particles resulting in slightly greater loss in streamwise stress intensity and deeper bed-normal stress penetration. In other words even though the average porosity for PR-DNS and VaNS cases is the same, the local porosity variations in the PR-DNS case create an uneven wall-blocking effect compared to the VaNS model, which has a uniform wall-blocking effect. This can be observed from the gradient of change for the stresses from their peak locations near the crest into the bed. The peaks in $\langle u'^2 \rangle^+$ (figure 5b) for the PR-DNS case happen slightly above the crest and the slope of change of the stress value is steeper, whereas for the VaNS model, the peak happens below the crest and the slope of change is shallower, similar slope behavior can also be observed in $\langle v'^2 \rangle^+$ (figure 5c). For the smooth wall case, turbulent fluctuations into the wall (i.e., sweeps) are redirected into wall parallel components due to the wall blocking effect resulting in greater tangential spread of the streamwise stress and lower peak in wall-normal stress away from the solid wall in the free stream. The Reynolds stress $\langle u'v' \rangle^+$ (figure 5d) is higher for the permeable bed cases compared to the smooth wall indicating that bed permeability and roughness enhance shear stress. Finally, the locations of the peak value of Reynolds stress and change of slope are observed below the crest for both permeable cases as compared to the smooth wall case.

Finally, figure 6 shows the normalized mean square pressure fluctuations, $\langle p'^2 \rangle^+$, for the PB-DNS, IWF-DNS, PB-VaNS, and SW cases. The pressure fluctuation magnitudes

and peak locations for the PB-DNS and IWF-DNS match well. The fluctuations quickly decay for $y/\delta < -0.5$, indicating that majority of the pressure fluctuations of significant magnitude are restricted to the top layer of the sediment bed. This suggests that the roughness elements of the top layer of sediment can capture the pressure variations well. Importantly, the peak value predicted by the PB-VaNS model is lower than the pore-resolved case, clearly showing the influence of the roughness protrusions in the top layer enhancing the turbulent pressure fluctuations. However, all these cases result in peaks that occur underneath the crest compared. For the SW-DNS, the peak pressure fluctuations are much smaller and occur at $y^+ \sim 30$ (above the solid wall). These results suggest that the porosity variation in the VaNS model should be altered to capture the effect of the top layer protrusions by incorporating variations in the spanwise and axial directions.

CONCLUSIONS

Direct numerical simulations are performed for a turbulent open channel flow over a porous sediment bed at permeability Reynolds number of $Re_k \sim 2.56$ ($Re_\tau=270$) representative natural stream or river system. The flow characteristics in a permeable bed are compared with an impermeable, rough wall with roughness elements representative of the top layer of the sediment bed. The predictive capability of an upscaled, continuum approach based on volume averaged Navier-Stokes (VaNS) equations is also evaluated by defining a smoothly varying porosity across the bed interface. The drag force in the VaNS approach was modeled using a modified Ergun equation with Forchheimer corrections for inertial terms (Wood *et al.*, 2020; Breugem *et al.*, 2006). The time-space averaging methodology is used to compute the mean velocity and Reynolds stresses. Differences in the near-bed turbulence structure, fluid shear stress acting on sediment bed, and turbulent pressure fluctuations were quantified.

The upscaled, PB-VaNS model captures the mean velocity and Reynolds stresses well as compared to the particle-resolved DNS data for the permeable bed (PB-DNS) as well as the impermeable, rough wall (IWF-DNS). The majority of turbulent pressure fluctuations occur within the top layer of the sediment bed and quickly decay within the bed. The PB-VaNS model captures the general trend in pressure fluctuations, but under predicts their magnitudes. This is attributed to the effect of roughness protrusions on the flow, which are absent in the PB-VaNS model but present in particle-resolved DNS. The local porosity variations in PB-DNS and IWF-DNS create a spatially varying wall-blocking as opposed to nearly uniformly wall-blocking effect in the PB-VANS model, resulting in the magnitude differences near the crest.

The above findings show that an upscaled, continuum approach, based on volume-averaged Navier-Stokes equations, is capable of accurately predicting various primary and secondary statistics for turbulent flow over flat sediment bed, in comparison to high fidelity pore-resolved DNS simulation. Streamwise and spanwise variations in porosity at the SWI, representative of the particle protrusions in the top sediment layer, may further improve the predictions of the PB-VANS model, and should be investigated in the future. The upscaled, PB-VaNS model is significantly faster than the pore-resolved simulations and can be easily extended to large-eddy simulations for reach-scale mass and momentum transport.

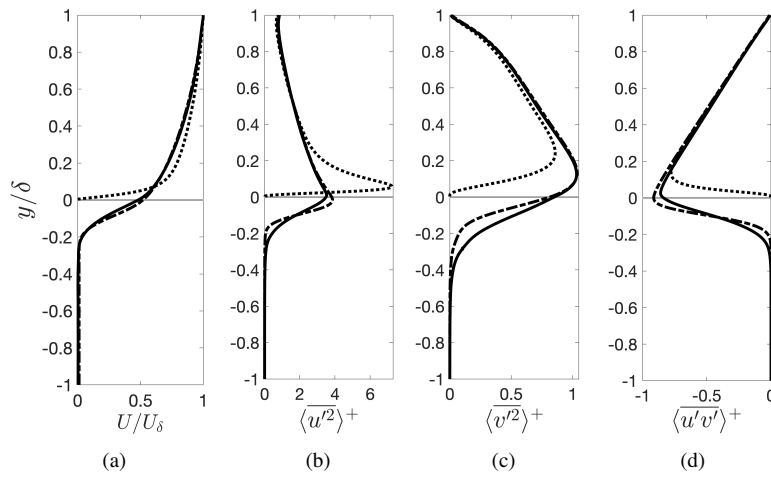


Figure 5. Comparison of the mean velocity and turbulent stress profiles for PB-VaNS model (---), PB-DNS (—), and SW-DNS (···) cases: (a) mean velocity and (b-d) streamwise, wall-normal, and shear components of Reynolds stress tensor. Horizontal gray line (—) shows the crest of sediment bed for PR-DNS and VaNS model and the underlying no-slip wall for the SW case.

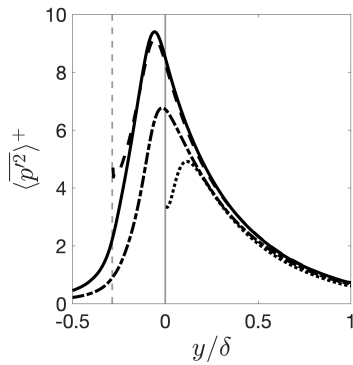


Figure 6. Profiles of mean-square pressure fluctuations $\langle p'^2 \rangle^+$ for PB-VaNS model (---), PB-DNS (—), IWF-DNS (- -), and SW (···) cases. Pressure is normalized by ρu_τ^2 . Solid gray vertical line (—) shows the crest of sediment bed and the dotted gray line (- -) shows the underlying no-slip solid surface in the IWF-DNS case.

ACKNOWLEDGMENTS

Authors gratefully acknowledge funding from US Department of Energy under award number DE-SC0021626 as well as US National Science Foundation award #205324. This research is part of the Frontera computing project at the Texas Advanced Computing Center. Frontera is made possible by National Science Foundation award OAC-1818253.

REFERENCES

Apte, S. V., Martin, M. & Patankar, N. A. 2009 A numerical method for fully resolved simulation (FRS) of rigid particle-flow interactions in complex flows. *Journal of Computational Physics* **228** (8), 2712–2738.

Breugem, WP, Boersma, BJ & Uittenbogaard, RE 2006 The influence of wall permeability on turbulent channel flow. *Journal of Fluid Mechanics* **562**, 35.

Grant, Stanley B., Gomez-Velez, Jesus D. & Ghisalberti, Marco 2018 Modeling the effects of turbulence on hyporheic exchange and local-to-global nutrient processing in streams. *Water Resources Research* **54** (9), 5883–5889.

Hester, Erich T, Cardenas, M Bayani, Haggerty, Roy & Apte, Sourabh V 2017 The importance and challenge of hyporheic mixing. *Water Resources Research* **53** (5), 3565–3575.

Karra, S 2023 Turbulent flows over permeable and impermeable sediment beds: Pore-resolved simulations and up-scaled modeling. PhD thesis, Oregon State University.

Karra, Shashank K, Apte, Sourabh V, He, Xiaoliang & Scheibe, Timothy D 2023 Pore-resolved investigation of turbulent open channel flow over a randomly packed permeable sediment bed. *Journal of Fluid Mechanics* **971**, A23.

Karra, Shashank K, He, Xiaoliang, Apte, Sourabh & Scheibe, Timothy D 2022 Particle resolved dns study of turbulence effects on hyporheic mixing in randomly packed sediment beds. In *Proceedings Of TSFP-12 (2022) Osaka*.

Macdonald, IF, El-Sayed, MS, Mow, K & Dullien, FAL 1979 Flow through porous media—the ergun equation revisited. *Industrial & Engineering Chemistry Fundamentals* **18** (3), 199–208.

Nikora, Vladimir, Koll, Katinka, McEwan, Ian, McLean, Stephen & Dittrich, Andreas 2004 Velocity distribution in the roughness layer of rough-bed flows. *Journal of Hydraulic Engineering* **130** (10), 1036–1042.

Rosti, Marco E, Cortelezzi, Luca & Quadrio, Maurizio 2015 Direct numerical simulation of turbulent channel flow over porous walls. *Journal of Fluid Mechanics* **784**, 396–442.

Voermans, JJ, Ghisalberti, M & Ivey, GN 2017 The variation of flow and turbulence across the sediment–water interface. *Journal of Fluid Mechanics* **824**, 413–437.

Whitaker, Stephen 1996 The forchheimer equation: a theoretical development. *Transport in Porous media* **25** (1), 27–61.

Wood, Brian D, He, Xiaoliang & Apte, Sourabh V 2020 Modeling turbulent flows in porous media. *Annual Review of Fluid Mechanics* **52**, 171–203.